

Atomically Dispersed MnN₄ Catalysts via Environmentally Benign Aqueous Synthesis for Oxygen Reduction: Mechanistic Understanding of Activity and Stability Improvements

Mengjie Chen,^{†,∇} Xing Li,^{‡,≠,∇} Fan Yang,^{⊥,∇} Boyang Li,[#] Thomas Stracensky,^{||} Stavros Karakalos,[§] Sanjeev Mukerjee,^{||} Qingying Jia,^{||} Dong Su,[‡] Guofeng Wang,^{*,#} Gang Wu,^{*,†} and Hui Xu^{*,⊥}

[†]Department of Chemical and Biological Engineering, University at Buffalo, The State University of New York, Buffalo, New York 14260, United States.

[‡]Center for Functional Nanomaterials, Brookhaven National Laboratory, Upton, New York 11973, United States.

[⊥]Giner Inc., Newton, Massachusetts 02466, United States

[#]Department of Mechanical and Materials Engineering, University of Pittsburgh, Pittsburgh, PA 15261, United States.

[§]Department of Chemical Engineering, University of South Carolina, Columbia, South Carolina 29208, United States.

^{||}Department of Chemistry and Chemical Biology, Northeastern University, Boston, Massachusetts, 02115, United States.

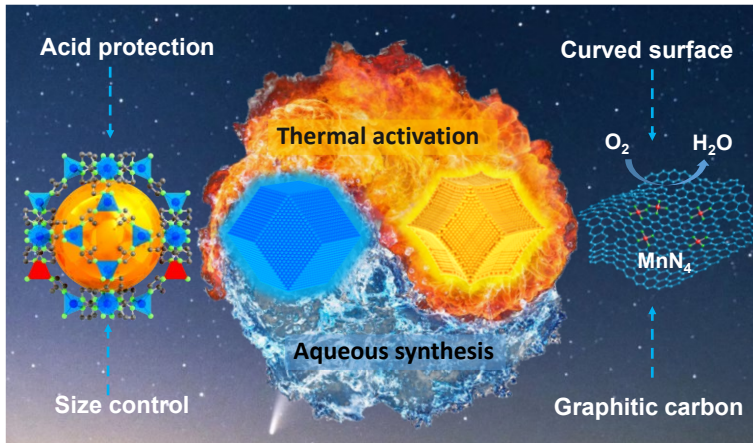
[≠]Key Laboratory of Materials Physics of Ministry of Education, School of Physics and Microelectronics, Zhengzhou University, Zhengzhou, 450052, China

*Corresponding authors

[∇]These authors contributed equally to this work.

Keywords: *PGM-free catalysts; single metal sites; Mn catalysts; electrocatalysis; oxygen reduction.*

TOC



Abstract: Development of platinum group metal (PGM)-free and iron-free catalysts for the kinetically sluggish oxygen reduction reaction (ORR) is crucial for proton-exchange membrane fuel cells (PEMFCs). A major challenge is their insufficient performance and durability in the membrane electrode assembly (MEA) under practical hydrogen-air conditions. Herein, we report an effective strategy to synthesize atomically dispersed Mn-N-C catalysts from an environmentally benign aqueous solution, instead of traditional organic solvents. This innovative synthesis method yields an extremely high surface area for accommodating an increased density of MnN₄ active sites, which was verified by using advanced electron microscopy and X-ray absorption spectroscopy. The new Mn-N-C catalyst exhibits promising ORR activity along with significantly enhanced stability, achieving a peak power density of 0.39 W cm⁻² under 1.0 bar H₂-air condition in MEA, outperforming most PGM-free ORR catalysts. The improved performance is likely due to the unique catalyst features, including curved surface morphology and dominant graphitic carbon structure, thus benefiting mass transport and improving stability. The first-principles calculations further elucidate the enhanced stability, suggesting that MnN₄ sites have a higher

resistance to demetallation than the traditional FeN₄ sites, during the ORR.

1. Introduction

Driven by the need to eliminate platinum group metal (PGM) catalysts, the research of PGM-free oxygen reduction reaction (ORR) cathode catalysts for proton-exchange membrane fuel cells (PEMFCs) has made unprecedented progress in the past decade.¹⁻⁴ Inspired by pioneering research,⁵⁻⁶ the carbon-based transition metal-nitrogen-carbon (M-N-C) catalyst (M: Fe, Co, or Mn) holds great promise due to their high intrinsic activity and reasonable stability for the ORR in acidic media.^{1, 7-8} Among all M-N-C catalysts, Fe-based catalysts demonstrated the most promising performance.⁹⁻¹³ However, the inferior durability of Fe-N-C catalysts in membrane electrode assemblies (MEAs) is still a substantial technical barrier for fuel cell transportation applications. Even worse, the H₂O₂ generated during the ORR reacts with Fe³⁺/Fe²⁺ to form detrimental hydroxyl and hydroperoxyl radicals via Fenton reactions, which attack organic ionomers, membranes, and catalysts.¹⁴⁻¹⁶ Eventually, the severe performance loss and cell failure occur due to the chemical and mechanical degradation of the MEAs.¹⁷ Therefore, the Fe-based catalyst is not ideal for replacing PGM catalysts in PEMFCs.^{14, 18} Although Co-N-C catalysts can alleviate the Fenton reactions to a certain degree, its relatively low intrinsic activity, and high cost remain grand challenges.¹⁹ Therefore, Mn-based catalysts that are low cost and have negligible activity towards the Fenton reactions are desirable PGM-free catalysts. In our previous works, we had experimentally and theoretically demonstrated the effectiveness to generate a high density of MnN₄ active sites embedded in a carbon phase, exhibiting promising catalytic activity and stability.²⁰⁻²¹ However, the Mn-N-C catalyst showed limited performance in a practical H₂-air fuel cell test with a low power density of 0.18 W cm⁻², which was far less than that of benchmark Fe-

N-C catalysts.²²⁻²⁴

The atomic MN_4 moieties, which are generally dispersed and embedded in micropores, are identified as ORR active sites, as evidenced by advanced spectroscopic characterizations and first-principles calculations.²⁵⁻²⁶ Like most of the other M-N-C catalysts, current Mn-N-C catalysts are derived from zinc-based zeolitic imidazolate frameworks (ZIF-8s), a subfamily of metal-organic frameworks (MOFs).²⁷ Because ZIF-8-derived carbon materials synthesized via carbonization at high temperature (*e.g.*, 1100 °C) possess an abundance of micropores and defects.²⁸⁻²⁹ The richness of micropores and defects is favorable for hosting a high density of MnN_4 sites with atomic dispersion in carbon. However, most of the ZIF-8 crystals are prepared from organic solvents such as methanol and dimethylformamide.³⁰⁻³¹ These organic solvents are toxic, costly, and potentially harmful to the environment, thus contradicting the sustainable concept of developing PGM-free catalysts for clean energy. Some reports have tried to circumvent this issue via solid-state synthesis of ZIF-8.³² These materials suffer from complicated procedures and heterogeneous morphology. In contrast, the synthesis of ZIF-8 in aqueous solutions would have many advantages including high efficiency, low cost, and being environmentally friendly.³³

Herein, we have developed a highly active Mn-N-C cathode catalyst from an aqueous solution synthesis method by using an acid-assisted step-pyrolysis strategy. This catalyst exhibits significantly enhanced activity and fuel cell performance, dramatically outperforming our previous Mn-N-C in 2018 by using dimethylformamide synthesis methods.²⁰ The new Mn-N-C catalyst achieved remarkable MEA performance, *i.e.*, the peak power density of 0.39 W cm⁻² under H₂-air. The homogeneous atomically dispersed MnN_4 active sites were directly confirmed by X-ray absorption spectroscopy (XAS) and high-resolution scanning transmission electron microscopy (STEM) images along with electron energy loss spectroscopy (EELS). This unique aqueous

synthesis method yielded a predominantly microporous carbon structure with a unique curved surface morphology, which is beneficial for hosting MnN_4 moieties and improved mass transport. Enhanced stability was also achieved due to the robust nature of MnN_4 and the formation of a graphitic carbon structure with a high degree of curvature. Compared to FeN_4 , the higher resistance for metal leaching of MnN_4 moieties was further confirmed by density functional theory (DFT) calculation. This work provided a new concept to develop atomically dispersed single metal atom site catalysts by using environmentally friendly aqueous synthesis with improved catalyst performance relative to traditional organic solvent-based synthesis.

2. Results and discussion

2.1 Catalyst synthesis, structures, and morphologies.

Three different catalyst samples were synthesized and studied in this work (details can be found in the supporting information). Typically, Mn-doped ZIF-8 precursors were prepared and carbonized from different procedures. For the Mn-N-C-1100 catalyst, the precursors were synthesized in the absence of acid protection and directly heat-treated at 1100 °C (the first thermal activation), followed by adsorption procedure and second thermal activation. For the Mn-N-C-HCl-1100 catalyst, the precursors were synthesized with the addition of acid and directly heat-treated at 1100°C (the first thermal activation), followed by identical adsorption and second thermal activation. For the Mn-N-C-HCl-800/1100 catalyst, the precursors were synthesized with addition of acid and carbonized from a step-pyrolysis method, which involved holding the temperature at 800 °C for 2 hours and then elevate it to 1100 °C for 1 hour (the first thermal activation), followed by the same adsorption and a second thermal activation process. During the multiple-step synthesis, Mn-N-C catalysts prepared by the first thermal activation are labeled correspondingly as Mn-N-C-1100-first, Mn-N-C-HCl-1100-first, Mn-N-C-HCl-800/1100-first.

The novel aqueous system catalyst synthesis procedure is illustrated in **Figure 1a**. The initial Mn-doped ZIF-8 precursors were synthesized in a dilute HCl acid. One of the grand challenges for Mn-N-C synthesis is that Mn atoms tend to form inactive metallic compounds and oxides, instead of active single metal atom sites.^{20, 27} The addition of HCl acid mitigates the hydrolysis process, prevents the formation of manganese oxides/clusters, and generates more porous structures. Moreover, the aqueous synthesis method can significantly shorten the reaction time to form ZIF-8 crystals because their nucleation and crystallization rates in water are much faster than those in organic solvents. Based on the XRD pattern (**Figure S1a**), the crystal structure of the Mn-doped ZIF-8 precursor was similar to that of reported ZIF-8s,^{11, 34} further verifying the effectiveness of the aqueous solution to form well-defined ZIF-8 crystals. Next, the Mn-doped ZIF-8 precursors can be carbonized to create a porous carbon structure by evaporating zinc easily, and MnN₄ can be created via a high-temperature treatment. Thus, the subsequent thermal activation process has a profound effect on the activity of the ZIF-derived Mn-N-C catalysts. A step-pyrolysis strategy (*i.e.*, 800 and 1100 °C) was developed to significantly increase the density of active sites located in the micropores. For example, if the temperature is directly increased to 1100 °C skipping the intermediate 800°C step, a loss of MnN₄ sites will occur due to the collapse of the micropores. As displayed in **Figure S2**, the specific surface area of different catalysts follows this trend: Mn-N-C-HCl-800/1100-first > Mn-N-C-HCl-1100-first > Mn-N-C-1100-first, implying that the acid-assisted step-pyrolysis method can effectively increase the surface area. The Mn-N-C-HCl-800/1100-first catalyst exhibited higher micropore volume within a broader range than the other two catalysts due to less micropore collapse.

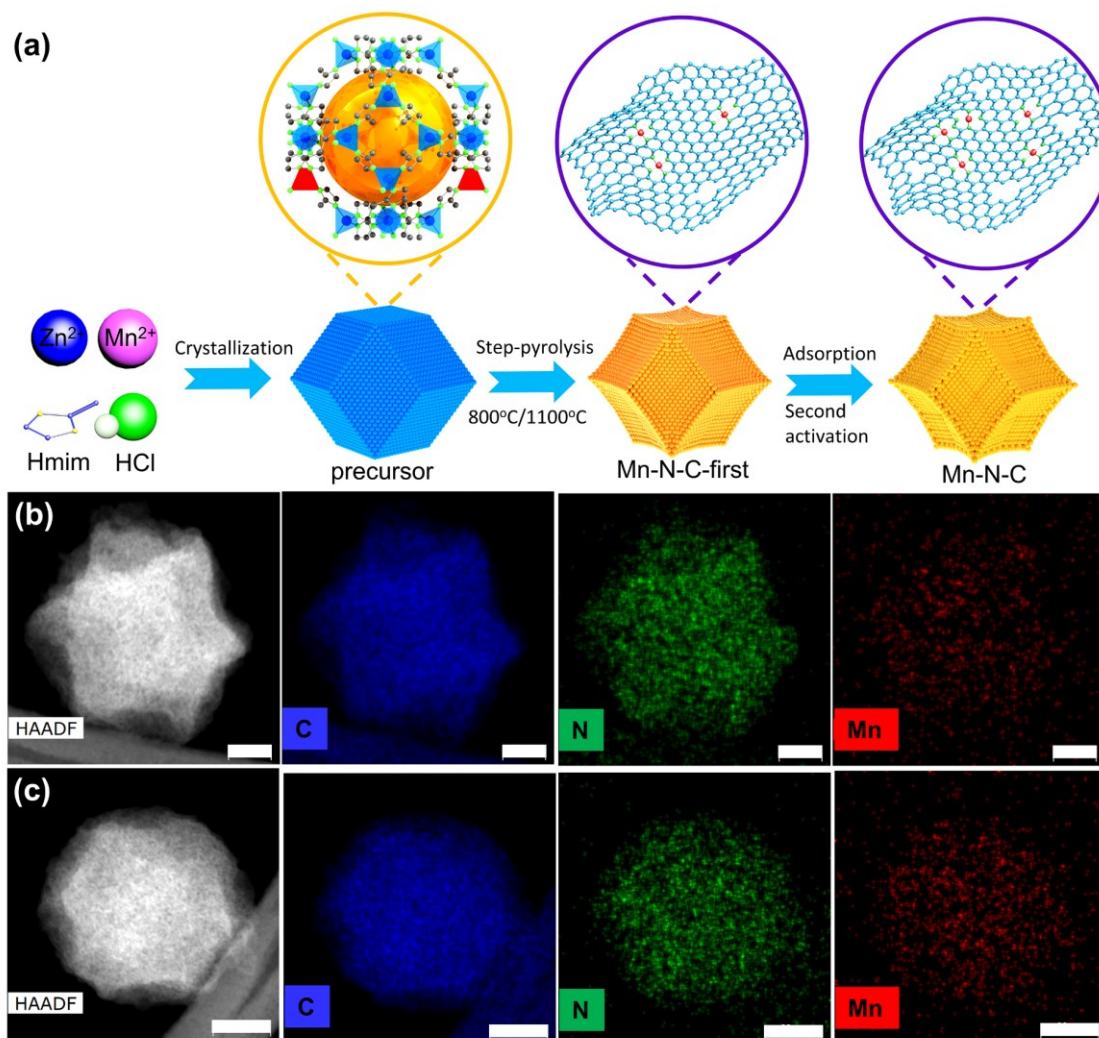


Figure 1. (a) Synthesis scheme for Mn-N-C catalysts and HAADF-STEM images with corresponding EDS elemental mappings of C, N, and Mn for (b) Mn-N-C-HCl-800/1100-first catalyst (scan bar: 20 nm) and (c) Mn-N-C-HCl-800/1100 catalyst after the second adsorption to introduce additional MnN_4 sites (scan bar: 30 nm).

The XRD patterns of the obtained catalyst show dominant peaks around 25° and 44° , which can be assigned to carbon planes (002) and (101), respectively (**Figure S1b**),³⁵ suggesting that the

Mn/ZIF precursors are well carbonized. Unlike the smooth surface often observed in catalysts from organic synthesis,^{16, 20, 34} the curved-surface polyhedron morphology of carbon particles is apparent in the catalyst obtained from the aqueous-based synthesis method (**Figures 1b** and **S3**). The curved surface morphology was created by the anisotropic thermal shrinkage of ZIF-8, where the vertices of the polyhedron are less stressed than the planar faces.⁹ Compared to organic solvents used for the synthesis, the much faster crystallization process in the aqueous solvent can lead to the formation of more defects, e.g., absence of nodes or linkers.³⁶ Thus, additional pore sizes are observed in the framework architecture and provide more space for the shrinkage of the ZIF-8 crystal.³⁷ Consequently, the edge frame of the polyhedron is retained while the planar faces collapse. The curved surface structure can improve the utilization of active sites at the surface by increasing the external surface area and exposing more active sites. It can also facilitate the mass transport by generating more mesopores and macropores.^{9, 38-39} To further increase the density of active sites, adsorption of Mn ions was performed on the Mn-N-C-HCl-800/1100-first catalyst followed by a second thermal activation. Unlike traditional Fe or Co-based catalysts, the Mn-based catalysts are very likely to form clusters during the one-step chemical doping, thus generating a very low density of MnN₄ active sites. To address this issue, we developed an effective two-step doping and adsorption method to introduce more active Mn sites into carbon catalysts step by step. The unique microporous structure and proper nitrogen doping of ZIF-derived carbon after the first step can serve as an ideal host to adsorb Mn ions sites in the second adsorption step and form more MnN₄ sites. The STEM-EDS elemental mapping displayed in **Figure 1b** and **1c** indicates that C, N, and Mn atoms are uniformly dispersed in the Mn-N-C-HCl-800/1100 catalyst. Notably, compared with the Mn-N-C-HCl-800/1100-first catalyst, the Mn signals became much denser and stronger in the final Mn-N-C-HCl-800/1100 catalyst, suggesting that the adsorption and second

thermal activation step can considerably increase the density of Mn sites.

2.2. ORR activity and stability.

The ORR activity and selectivity of these catalysts were evaluated by using a rotating ring-disk electrode (RRDE) in 0.5 M H₂SO₄ electrolyte at room temperature. The lower activity was observed for Mn-N-C catalysts derived from methanol and DMF, suggesting very less active MnN_x moieties in these catalysts (**Figure S4**), and the Mn ions cannot be chemically doped into ZIF crystals easily. Unlike traditional organic solvents, in which the Mn ions cannot coordinate with N ligands effectively during the chemical doping step, the Mn-N-C-HCl-800/1100-first catalyst derived from direct Mn-doped ZIF-8 in aqueous solution showed a more positive half-wave potential ($E_{1/2}$) of 0.69 V vs. RHE in 0.5 M H₂SO₄. H₂O molecules would partially break the coordination bonds between organic linkers and zinc nodes during nucleation and crystallization, exposing the unsaturated N sites for bonding with Mn ions.⁴⁰ Thus, more Mn ions can be coordinated with N sites to obtain a higher density of Mn-N₄ complexes in aqueous solution.

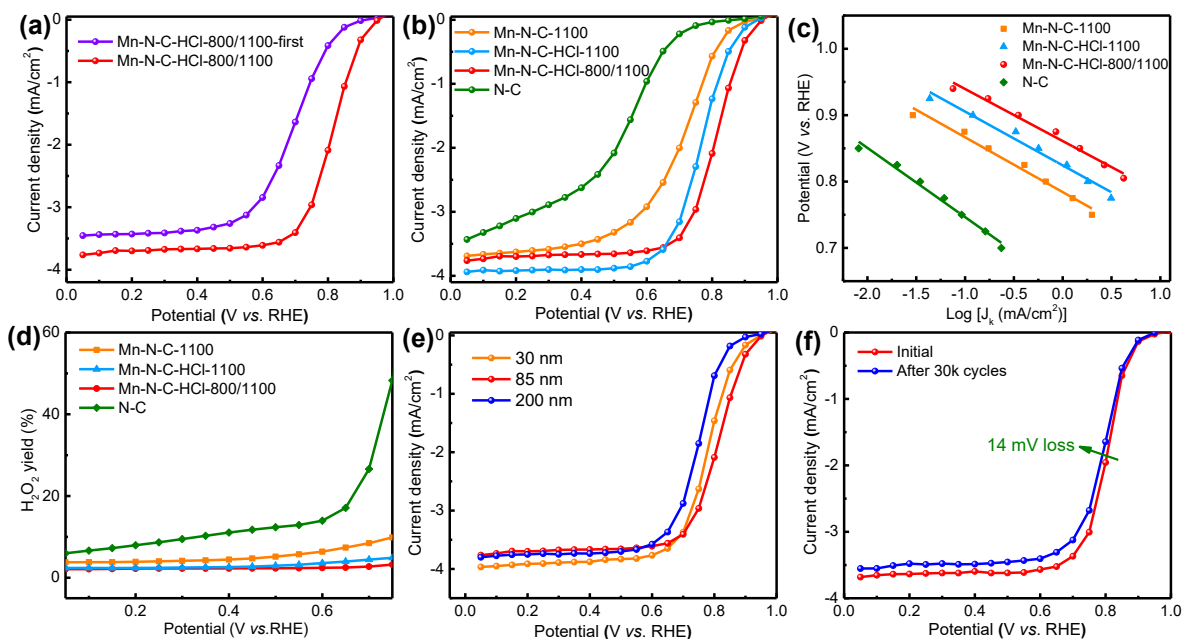


Figure 2. (a) Steady-state ORR polarization curves of Mn-N-C-HCl-800/1100-first and Mn-N-C-HCl-800/1100. (b) Steady-state ORR polarization curves of Mn-N-C-1100, Mn-N-C-HCl-1100, Mn-N-C-HCl-800/1100, and N-C. (c) Tafel plots of ORR on different catalysts replotted from the polarization curves. (d) Hydrogen peroxide yields of Mn-N-C-1100, Mn-N-C-HCl-1100, Mn-N-C-HCl-800/1100, and N-C. (e) Steady-state ORR polarization curves of Mn-N-C catalysts with various sizes. (f) Steady-state ORR polarization curves of Mn-N-C-HCl-800/1100 before and after potential cycling tests (0.6-1.0 V, 30,000 cycles).

Notably, zinc in ZIF-8 precursors starts to evaporate under 800 °C to generate a porous structure.¹⁰ Therefore, we chose 800 °C as the critical temperature for the carbonization of Mn-doped ZIF-8 precursors in the first period of the step-pyrolysis process. The poor RDE performance (**Figure S5**) indicates that there is no formation of MnN_x active sites during the first period of step-pyrolysis. However, after the first period of step-pyrolysis, nitrogen defects were exposed due to zinc evaporation. Then the temperature was further elevated to 1100 °C to facilitate the diffusion of Mn ions and the generation of MnN₄ active sites. Followed by adsorption and the second thermal activation, the Mn-N-C-HCl-800/1100 catalyst showed significantly enhanced activity compared with Mn-N-C-HCl-800/1100-first, proving that more accessible active sites were introduced (**Figure 2a**). This activity improvement is in good agreement with the results of STEM-EDS mapping showing an increased atomic Mn signal in the final catalyst. The adsorption and the second thermal activation steps can dramatically improve the activity for all Mn catalysts (**Figure S6**).

As shown in **Figure 2b**, the Mn-N-C-1100 catalyst synthesized without the assistance of acids exhibited inferior ORR activity due to the formation of manganese oxides (**Figure S7**), which

undermined the surface area (**Figure S8** and **Table S1**) and inhibited the formation of MnN_4 active sites. With acid assistance, the Mn-N-C-HCl-1100 catalyst showed improved activity, which can be attributed to the higher density of active sites and a more porous structure. No manganese oxides/clusters are detected in the Mn-N-C-HCl-1100 catalyst, indicating that the acid plays a crucial role in isolating the Mn ions and avoiding the formation of manganese oxides. The best performing Mn-N-C-HCl-800/1100 catalyst showed the highest activity with an $E_{1/2}$ of 0.815 V *vs.* RHE as well as the highest surface area ($>1500 \text{ m}^2 \text{ g}^{-1}$). The micropore area is the principal key factor in improving ORR activity by accommodating the active sites.⁴¹⁻⁴³ Therefore, the abundant micropores ($0.52 \text{ cm}^3 \text{ g}^{-1}$) in the Mn-N-C-HCl-800/1100 catalyst is favorable for hosting a high density of active sites. The previously reported 20Mn-NC-second catalyst²⁰ was compared with our new Mn-N-C-HCl-800/1100 catalyst (**Figure S9**). The Mn-N-C-HCl-800/1100 catalyst exhibited a current density higher by three times than that of the 20Mn-NC-second catalyst at 0.9 V. Given that less Mn content was observed for the Mn-N-C-HCl-800/1100 catalyst (**Table S2**), the higher activity can be attributed to the higher utilization of MnN_4 moieties at the surface due to the unique curved-surface structure. The activity of the Mn-free nitrogen-doped carbon (N-C) catalyst was also tested under the same condition, which only showed a half-wave potential around 0.53 V (**Figure 2b**), suggesting that the formation of Mn-related active sites is essential for the high ORR activity. As shown in **Figure 2c** and **Table S3**, Tafel slopes ranging from 75 to 85 mV dec^{-1} were determined for Mn-based catalysts, suggesting that the mixed control on rate-determining step involves the transfer of the first electron (60 mV dec^{-1}) and the diffusion of intermediates at catalyst surfaces (118 mV dec^{-1}).⁴⁴⁻⁴⁶ Among all Mn-N-C catalysts, the Mn-N-C-HCl-800/1100 catalyst showed the lowest Tafel slope, indicating the fastest ORR kinetics. The Mn-free nitrogen-doped carbon catalyst demonstrated a much higher Tafel slope (104 mV dec^{-1})

at low currents, indicating a different reaction mechanism and much slower kinetics. Moreover, the Mn-N-C-HCl-800/1100 catalyst yielded insignificant hydrogen peroxides (less than 3%) during the ORR, suggesting good selectivity of the four-electron pathway (**Figure 2d**). In this study, Mn-N-C-HCl-800/1100 catalysts with different particle sizes were also prepared and compared, in which 85 nm catalyst demonstrated the highest performance (**Figure 2e**). This can be attributed to the fact that higher microporosity and specific surface area were observed for the 85 nm catalyst, which in turn facilitated the exposure and utilization of active sites.

The stability of Mn-based catalysts was also evaluated via accelerated stress tests (potential cycling from 0.6 to 1.0 V) in O₂-saturated 0.5 M H₂SO₄ during the ORR. The best performing Mn-N-C-HCl-800/1100 catalyst demonstrated excellent stability with a loss of 14 mV in $E_{1/2}$ after 30,000 cycles (**Figure 2f**). The stability is significantly enhanced when compared to other ZIF-8 derived Fe-N-C and Co-N-C catalysts,^{11, 15-16} indicating the Mn-N-C catalyst holds promise to address the stability issue of PGM-free ORR catalysts. For comparison, the Mn-N-C-HCl-1100 catalyst (without step-pyrolysis) was subject to the identical stability test. The Mn-N-C-HCl-1100 catalyst was found to be less stable (**Figure S10**), suggesting that the step-pyrolysis strategy can improve stability by modifying the carbon structure. Compared with the Mn-N-C-HCl-1100 catalyst, the Mn-N-C-HCl-800/1100 catalyst demonstrated less change of capacitance and a more graphitic carbon structure due to the longer duration of heat-treatment and modulated temperature (**Figure S11**).

2.3. Mechanistic understanding of activity and stability improvements

The electrochemical performance dependence on catalyst size was investigated and displayed in **Figure 3**. Herein, as displayed in **Figure S12**, the size of Mn-doped ZIF precursors was tuned

through varying the concentration of chemicals (*i.e.*, 2-methylimidazole). Thus, the particle size of various catalysts can be adjusted and prepared. After the carbonization, the dominant rhombic polyhedron shape of Mn-doped ZIF-8 was retained except that the catalyst particle was shrunk, and the particle surface became irregular. Following the adsorption and the second thermal activation, the catalyst maintained a similar size as it was in the first step (**Figure 3a**). XRD results indicate all Mn-N-C catalysts showed a similar crystal carbon structure (**Figure 3b**). From the Raman spectra (**Figure 3c**), all catalysts exhibited similar ratios of D and G peak areas ($\text{Area}_D/\text{Area}_G$), where the ratio of the relative intensity of D to G band can be an indicator of the graphitization degree of the carbon structure.⁴⁷⁻⁴⁸ The N₂ sorption isotherms (**Figure 3d**) of the various Mn-N-C catalysts, used to determine the Brunauer-Emmett-Teller (BET) surface areas, provide a discerning factor for catalytic activity. As shown in **Figure 2e**, the catalytic activity of Mn catalysts follows a trend: 85 nm > 30 nm > 200 nm, which is consistent with the trend of specific surface area. The high surface area can be mainly ascribed to the dominant microporosity, evidenced by the gradual increase in the N₂ uptake at low pressures. The best performing 85 nm catalyst also exhibited the highest surface area (1511 m² g⁻¹). The 200 nm catalyst demonstrated the lowest activity with a surface area of 923 m² g⁻¹. The catalytic activity, surface areas, and particle sizes are well correlated in **Figure S13** and **Table S4**.

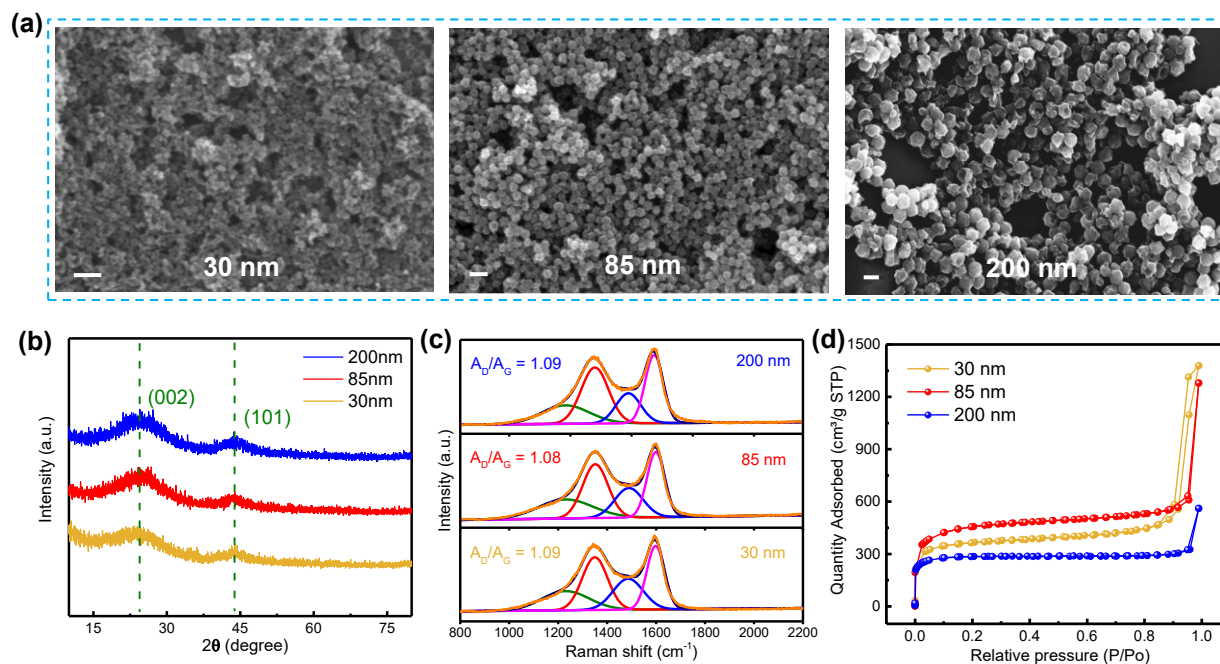


Figure 3. (a) SEM images of Mn-N-C catalysts with various particle sizes. Scan bar: 200 nm. (b) X-ray diffraction patterns of Mn-N-C catalysts with various sizes. (c) Raman spectra of Mn-N-C catalysts with various particle sizes. (d) N₂ sorption isotherms of Mn-N-C catalysts with various particle sizes.

The atomic-level structure and the chemistry of Mn-N-C catalysts were extensively studied by scanning transmission electron microscopy (STEM) images, electron energy loss spectroscopy (EELS), and XAS analysis. **Figure 4a** elucidated the overall morphology via a STEM image, and the Mn-N-C-HCl-800/1100-first catalyst exhibited a curved surface polyhedron structure. **Figure 4b** further showed the porous structure of the Mn-N-C-HCl-800/1100-first catalyst. The nitrogen-coordinated Mn sites (the bright dots in the red circles) can be visualized by using STEM (**Figure 4c**) along with EELS (**Figure 4d**). The advanced electron microscopy study verifies that atomically dispersed Mn sites are homogeneously embedded into the carbon matrix throughout the catalyst.

Furthermore, the Mn-N-C-HCl-800/1100-first catalyst was subject to an adsorption step and a second thermal activation, where the acid and urea were introduced to prevent the formation of Mn oxides/clusters and provide a source of additional nitrogen, respectively. Moreover, the hydrochloric acid can also activate the catalyst by improving the BET surface area and pore volume of carbon.⁴⁹⁻⁵⁰ HR-TEM images with electron diffraction patterns (**Figure S14**) confirm the existence of porous carbon structure, and the absence of Mn oxides or clusters in the catalysts, which are in good agreement with XRD results. Also, compared to the Mn-N-C-HCl-800/1100-first, the curved surface morphology of the Mn-N-C-HCl-800/1100 catalyst became more dominant (**Figure 4e**), and a more porous structure was achieved (**Figures 4f and S15**). The increased surface area can be attributed to the fact that the more dominant micropores formed after the adsorption and the second thermal activation (**Figure S16**), which is related to the pore formation induced by the uses of HCl and urea.^{49, 51} This is different from the results we observed previously, in which the specific surface area of catalysts was often reduced after the second thermal activation.²⁰ The higher micropore volume can accommodate more MnN₄ active sites in the second step, which has been verified by ORR activity enhancement and STEM elemental mapping (**Figures 1 and 2a**). The ammonia generated from the decomposition of urea could help to create more defects, thus increasing the density of MnN₄ sites.²⁶ The atomically dispersed nitrogen-coordinated manganese sites (the bright dots in red circles) in the final catalyst were also verified via HR-STEM (**Figure 4g**) and EELS (**Figure 4h**). Therefore, the improved ORR activity is due to increased surface area and density of MnN₄ active sites.

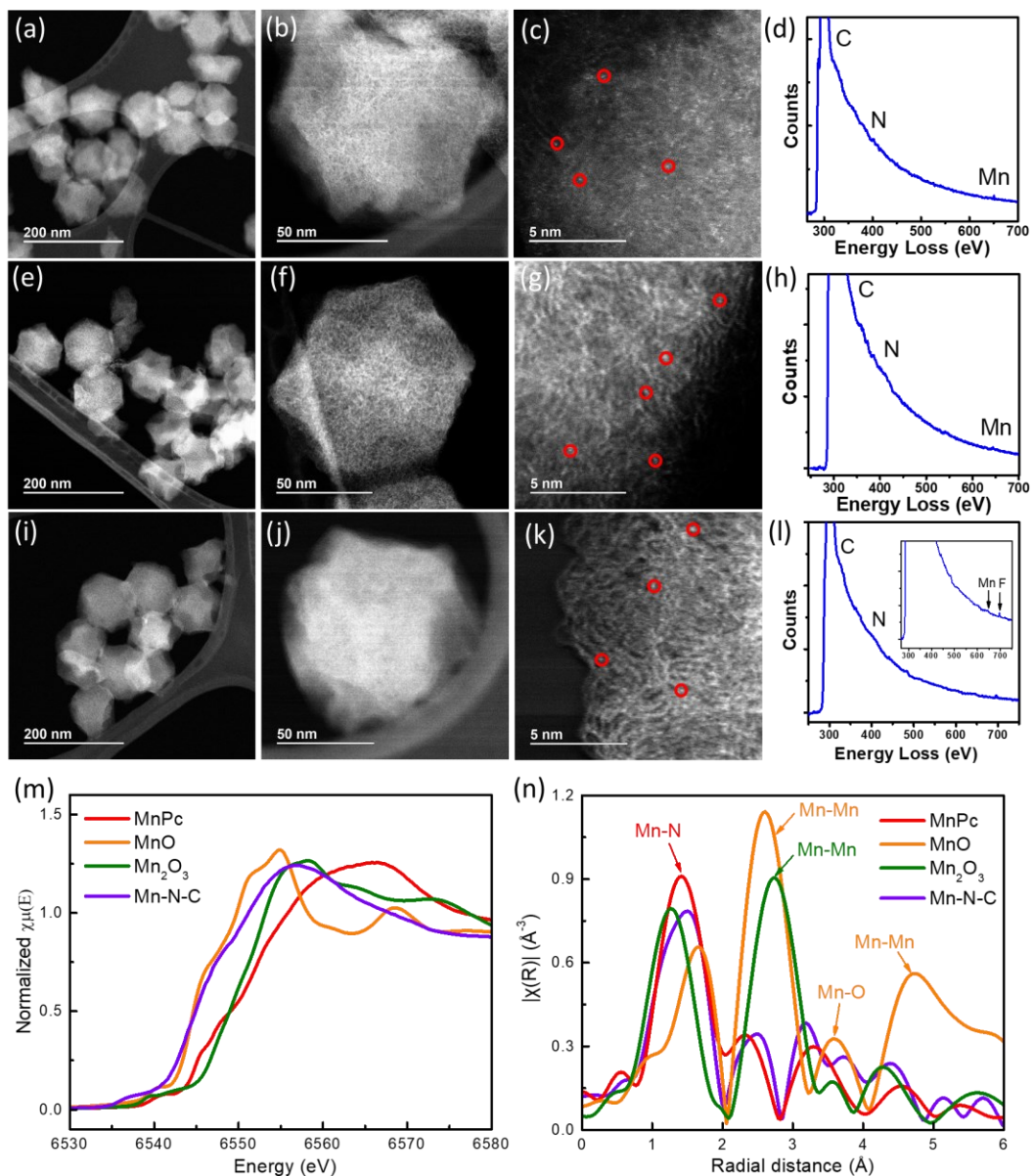


Figure 4. STEM images and corresponding electron energy loss spectroscopy of (a-d) Mn-N-C-HCl-800/1100-first, (e-h) Mn-N-C-HCl-800/1100, and (i-l) Mn-N-C-HCl-800/1100 after potential cycling (0.6-1.0 V, 30,000 cycles). (m) The K-edge XANES spectra of the Mn-N-C-HCl-800/1100 catalyst and standard samples (MnPc, MnO, and Mn₂O₃) and (n) Fourier-transformed-EXAFS spectra of the Mn-N-C-HCl-800/1100 catalyst and standard samples (MnPc, MnO, and Mn₂O₃).

The best performing Mn-N-C-HCl-800/1100 catalyst after the accelerated stress test was further studied by applying HADDF-STEM, and the images provide an underlying mechanistic understanding of stability enhancement (**Figures 4i-l** and **S17**). The curved surface of carbon architecture was retained after 30,000 potential cycles, suggesting excellent stability of catalysts in terms of carbon corrosion resistance. The carbon stability can be attributed to the formation of a curvature-shaped graphitic carbon structure (**Figure S18**).⁵²⁻⁵³ These graphitic carbon layers stacked in the Mn-N-C-HCl-800/1100 catalyst is possibly related to the step-pyrolysis method and further enhanced by the second thermal activation as the Mn-N-C-HCl-800/1100 catalyst shows a more dominant graphitic carbon structure when compared to the Mn-N-C-HCl-800/1100-first catalyst (**Figure S19**). The change of carbon structure was also confirmed by Raman spectroscopy, in which more graphitic carbon structures were detected from the Mn-N-C-HCl-800/1100 catalyst. The generation of such a high curvature graphitic carbon structure can start from 800 °C during the first period of the step-pyrolysis of the Mn-doped ZIF-8 precursor.⁵⁴ Notably, in traditional synthesis methods, the heat-treatment duration is usually short. Therefore, the carbonization of the precursor is insufficient to generate such a graphitic carbon structure. In this work, longer duration of heat treatments, modulated temperature, and additional second thermal activation can all facilitate the formation of such unique graphitic carbon structures. After potential cycling, the atomically dispersed nitrogen-coordinated Mn sites still retained in the carbon matrix, and no Mn clusters were observed, suggesting the robustness of the Mn-N coordination structure during the ORR in the acid media (**Figures 4k** and **4l**). This result is consistent with RDE observations.

XAS measurements further examined the Mn-N-C catalyst. Manganese phthalocyanine (MnPc), MnO, and Mn₂O₃ were also studied as standard Mn compounds for comparison. The bulk average oxidation state of the Mn in the Mn-N-C-HCl-800/1100 catalyst was estimated by the position of

the X-ray absorption near-edge structure (XANES) spectra. **Figure 4m** presents that edge position of the Mn K-edge XANES spectrum of the Mn-N-C-HCl-800/1100 catalyst nearly overlaps that of the MnO, indicating a bulk average oxidation state of +2. This is in good agreement with the XPS result (**Figure S20**), where the valence of Mn ions of the Mn-N-C-HCl-800/1100 catalyst was identified to be Mn²⁺ based on the binding energy of Mn 2p_{1/2} and Mn 2p_{3/2} situated at ca. 653.2 and 641.5 eV, respectively. The N 1s peak can be fitted into four peaks situated at 398.3, 399.3, 401.3, and 404.0 eV, which can be assigned to pyridinic-N, Mn-N species, graphitic-N, and oxidized-N, respectively. The nitrogen content and types are similar to traditional iron-based catalysts (**Table S2**). The pyridinic nitrogen can act as anchor sites to coordinate with Mn sites. Moreover, the graphitic nitrogen was the dominant species observed in our catalysts, which can modify the electronic structure of carbon materials by delocalizing the electron distribution of carbon planes to improve the ORR kinetics.⁵⁵ Moreover, the d-orbital filling and spin of transition metal center can be significantly impacted by surrounding graphitic N, leading to the improved intrinsic activity of MN₄ sites.⁵⁶ The local structures of Mn sites in the Mn-N-C-HCl-800/1100 catalyst and standard Mn compounds were also characterized by an extended X-ray absorption fine structure (EXAFS) analysis. The Fourier-transformed (FT) EXAFS spectrum of the Mn-N-C-HCl-800/1100 exhibited a predominant peak of around 1.5 Å (**Figure 4n**), which can be attributed to the Mn-N/O first coordination shell.^{20, 57} The two scattering peaks of the MnO around 2.6 Å and 4.8 Å can be assigned to the Mn-Mn pathways.⁵⁸ Thus, the absence of such Mn-Mn peaks for the Mn-N-C-HCl-800/1100 indicates no Mn oxides cluster with long-range ordered structures. The EXAFS analysis agrees with the XRD and STEM results that the Mn exists as atomically dispersed single Mn site species. To further understand the chemical structure of Mn-N coordination, we characterized MnPc with a fingerprint MnN₄ structure as a standard baseline for possible active

site identification of the Mn-N-C-HCl-800/1100 catalyst (**Figure S21** and **Table S5**). It is noted that the FT-EXAFS of the Mn-N-C-HCl-800/1100 catalyst closely follows that of the MnPc up to 5 Å (**Figure 4n**), suggesting the presence of MnN₄ moieties in the Mn-N-C-HCl-800/1100 catalyst. The presence of Mn-O_x species cannot be conclusively excluded by XAS analysis since N and O as scattering neighbors cannot be distinguished by XAS, but the N coordination is supported by STEM and EELS analysis.

In previous studies²⁰⁻²¹, we employed the first-principles density functional theory (DFT) calculations to predict the intrinsic ORR activity of an MnN₄ site. The most likely active site contains a central Mn atom coordinated with four N atoms embedded in a graphene layer with a planar configuration. The MnN₄ site exhibits a thermodynamically favorable four-electron pathway for the ORR with a predicted limiting potential of 0.54 V and kinetically feasible activation energy of 0.37 eV for breaking the O-O bond during the OOH dissociation. Hence, these computational results well explained the observed activity of the Mn-N-C catalysts for the ORR. Here, we further performed the DFT calculations to model the metal leaching processes from both MnN₄ and FeN₄ sites to attain an understanding of the observed stability improvement of the Mn-N-C catalysts. Calculated Pourbaix diagrams show that these clean MnN₄ and FeN₄ sites are thermodynamically stable only under low electrode potential ($U < 0.5$ V vs. RHE) in acid media.⁵⁹ Under electrode potential higher than 0.5 V, the MnN₄ site was predicted to be terminated by an oxygen atom, whereas the FeN₄ site terminated by a hydroxyl group. The different stable states of the MnN₄ and FeN₄ sites during ORR at high potential is a result of the lower thermodynamic driving force for O protonation reaction to form OH on MnN₄ than on FeN₄ site. The adsorption of an oxygen molecule (O₂) on the central metal of these active sites is the first and inevitable step of the ORR. Consequently, we compare in this work the stability against metal leaching of the

clean, oxygen-species terminated, and oxygen-molecule adsorbed MnN_4 and FeN_4 sites, as shown in **Figure 5** and **Figure S22**, respectively.

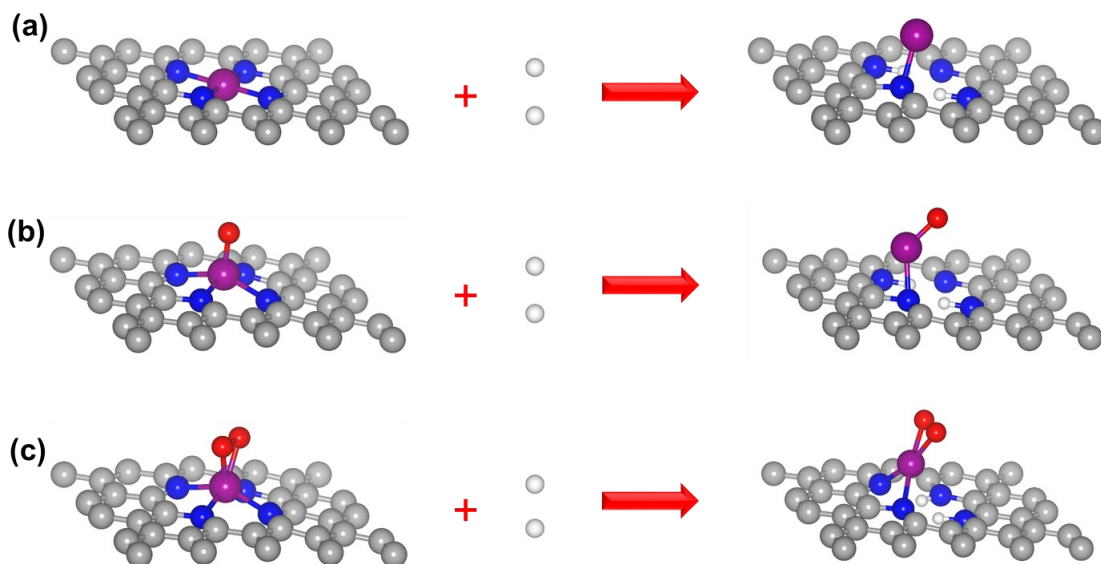


Figure 5. Atomistic models showing the leaching of central Mn metal from (a) an MnN_4 site, (b) oxygen terminated MnN_4 site, and (c) an oxygen molecule adsorbed MnN_4 site. In the figure, the gray, blue, purple, red, and white balls represent C, N, Mn, O, and H atoms, respectively.

Also shown in **Figure 5**, we assume that the change of free energy could gauge the tendency of metal leaching from a metal- N_4 site when two protons replace the central atom and hence loses its four N coordination. The free energy change for these processes can be calculated by comparing the energies before and after the metal leaching and considering the free energy of proton as $1/2\text{H}_2$ gas in acid media. Namely, a positive value of the free energy change indicates a barrier, whereas a negative value indicates a spontaneous process for the metal leaching process. We presented our DFT calculation results in **Table 1**. For clean MnN_4 and FeN_4 sites, we predict that the metal leaching has a high free energy barrier (2.98 eV for MnN_4 and 3.38 eV for FeN_4).

Table 1. Free energy changes for the leaching of the central metal atom from MnN₄ and FeN₄ sites calculated from DFT.

Free energy change (eV)	Clean	Oxygen species-terminated	Oxygen molecule-adsorbed
MnN ₄	2.98	1.84	0.86
FeN ₄	3.38	1.33	0.76

These results indicate that it is challenging to lose metal from the clean MnN₄ and FeN₄ sites. Hence, we believe that the metal leaching process from the clean metal-N₄ sites might have a negligible impact on the stability of the catalysts. In contrast, **Table 1** shows that the free energy changes for the metal leaching from the oxygen-species (O or OH) terminated and oxygen-molecule adsorbed MnN₄ and FeN₄ sites are comparatively lower, suggesting that these two processes would contribute significantly to the observed instability of these catalysts. Our DFT results indicate that the oxygen-species terminated MnN₄ is about 1.84 eV, more stable than the oxygen-species FeN₄ site at 1.33 eV. Also, the oxygen-molecule adsorbed MnN₄ is about 0.10 eV more stable than the oxygen-molecule adsorbed FeN₄ site. Thus, our DFT calculations provide a mechanistic understanding of the experimentally observed stability improvement of the Mn-N-C catalysts as compared to the Fe-N-C catalysts.

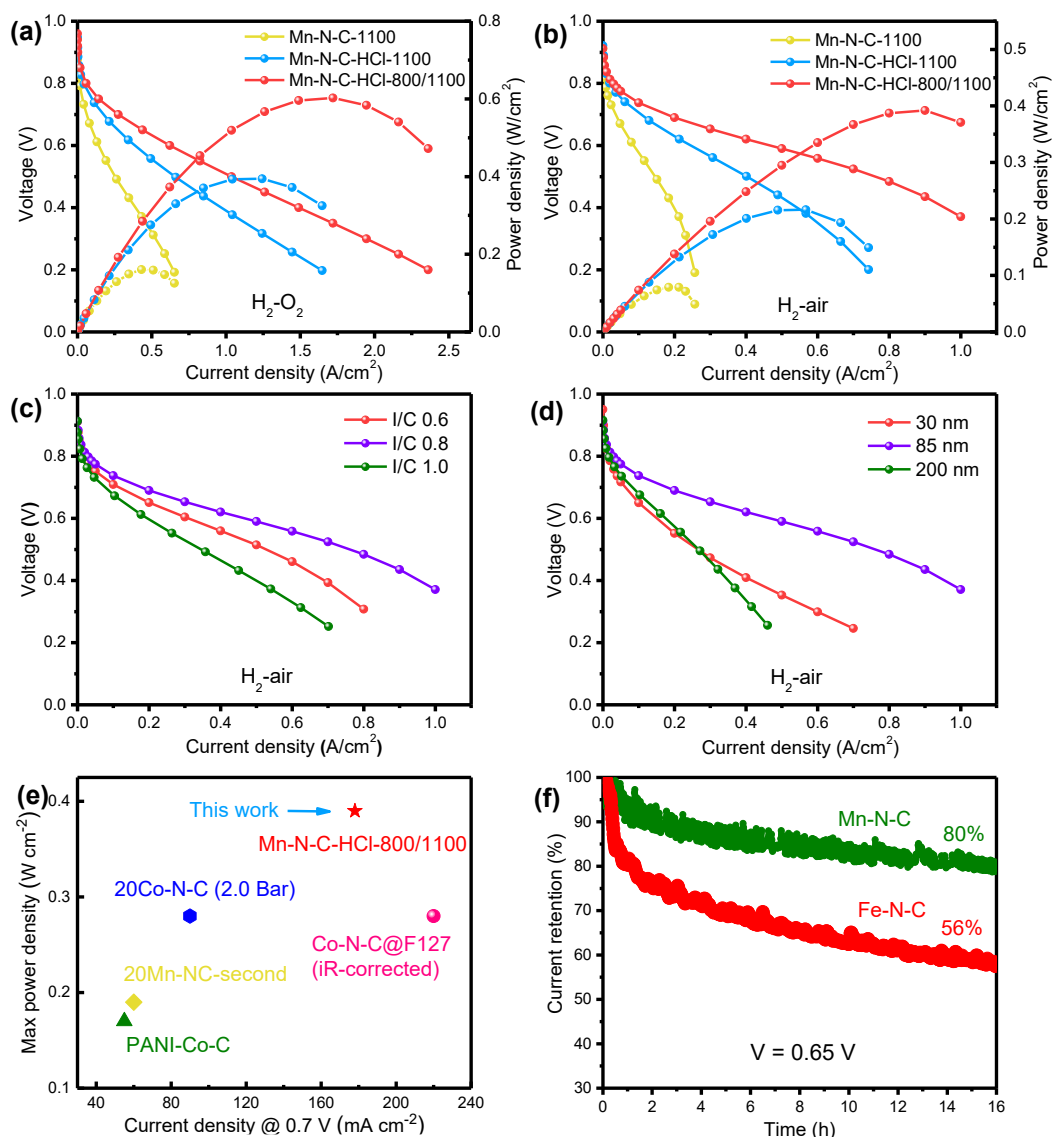


Figure 6. (a) Fuel cell performance of different catalysts under H₂-O₂. Cathode: 4.0 mg cm⁻²; O₂ flow rate 1000 sccm; 100% RH; 1 bar O₂ partial pressure; anode: 0.3 mg_{Pt} cm⁻² Pt/C; H₂ flow rate 200 sccm; 100% RH; membrane: Nafion[®] 212. (b) Fuel cell performance of various catalysts under H₂-air. Cathode: 4.0 mg cm⁻²; air flow rate 1000 sccm; 100% RH; 1 bar air partial pressure; anode: 0.3 mg_{Pt} cm⁻² Pt/C; H₂ flow rate 200 sccm; 100% RH; membrane: Nafion[®] 212. (c) Polarization curves of Mn-N-C-HCl-800/1100 catalyst with various I/C ratio at 100% RH under H₂-air conditions (d) Polarization curves of Mn-N-C catalysts with different particle size. All polarization

curves are not iR corrected. (e) Maximum power density and current density @ 0.7 V of iron-free cathode catalysts for PEMFC under H₂-air conditions at 80 °C and 100% RH. (1.0 bar total partial pressure and not iR corrected unless specified) (f) Fuel cell durability tests of Mn-N-C and Fe-N-C at a constant potential of 0.65 V under H₂-air conditions.

2.4 MEA performance

Owing to the significant differences in temperature, acidity, pressure, proton/electron conductivity, and electrode structures between RDEs and MEAs, it is challenging to transfer high activities of PGM-free catalysts into MEA performance directly.⁷ At first, the fabricated MEA was investigated under the H₂-O₂ condition (**Figure 6a**). As expected, the Mn-N-C-1100 catalyst showed poor performance in the whole current range due to the inferior intrinsic activity of Mn oxides, which also reduced the number of Mn-N active sites and blocked the micropores. Moreover, the Mn-N-C-1100 catalyst showed a tendency to agglomerate together with a smaller primary particle size (**Figure S23**), which can block the dispersion and distribution of ionomer. Compared with the Mn-N-C-1100 catalyst, the performance of the Mn-N-C-HCl-1100 catalyst was improved in the whole current range, indicating the removal of Mn oxides by using HCl can enhance the activity and change the carbon structure of the catalyst. However, the Mn-N-C-HCl-1100 catalyst also showed poor mass transport due to insufficient mesopores and macropores, even though primary particles of the Mn-N-C-HCl-1100 were well isolated and form less large aggregates. With the step-pyrolysis, the MEA performance of the Mn-N-C-HCl-800/1100 catalyst was significantly improved. It achieved an OCV of 0.95 V, which was comparable to that of our previously reported 20Mn-NC-second catalysts.²⁰ Meanwhile, the achieved maximum power density of the Mn-N-C-HCl-800/1100 cathode was 0.6 W cm⁻², which was much higher than that

of the 20Mn-NC-second catalyst (**Figure S24**). More importantly, the current density at 0.8 V for the Mn-N-C-HCl-800/1100 catalyst was about 1.5 times higher than that of the 20Mn-NC-second catalyst, indicating that more active sites were exposed and utilized under the same condition likely due to a more porous structure of the Mn-N-C-HCl-800/1100 catalyst.

The performance of the catalyst was also investigated under practical H₂-air conditions (**Figure 6b**). Due to the mass transport limitation in the air, the performance gap among the different catalysts became more apparent. The OCV of the Mn-N-C-HCl-800/1100 was 0.91 V, which was comparable to other reported iron-free cathode catalysts.^{15, 20} More importantly, the maximum power density was 0.39 W cm⁻² under 1.0 bar pressure of H₂/air, which outperformed all Fe-free cathode catalysts and was comparable with iron-based catalysts. The achieved power density was two times higher than that of our previously reported 20Mn-NC-second catalysts (**Figure S24**). The significantly enhanced performance at a high current density region is due to dramatically enhanced mass transport. The curved surface structure likely favors the formation of abundant mesopores/macropores, which can enhance the mass transport and improves the utilization of active sites by facilitating ionomer dispersion and distribution.⁶⁰ This was verified by microscopy images of MEA structures, where the Mn-N-C-HCl-800/1100 catalyst layer exhibited a porous structure and uniform ionomer distribution. In contrast, large aggregates, dense structure, and high concentrated ionomer were observed for the previous 20Mn-NC-second catalyst layer.

The ratio of ionomer to catalyst was also modulated by preparing MEAs by using the best performing Mn-N-C-HCl-800/1100 catalyst (**Figure 6c**). The optimal I/C ratio is determined to be 0.8. The electrochemical surface area (ECSA) of catalysts can be measured to evaluate the number of active sites in contact with ionomer by impacting the ionomer dispersion and infiltration.⁶¹⁻⁶² In this study, when the ratio of I/C was increased from 0.6 to 0.8, both better ionomer coverage of the

catalyst and more ionomer infiltration into the catalyst layer were achieved. Thus, the contact area between the catalysts and ionomer was increased. The MnN₄ active sites can participate in the ORR only when located at the three-phase boundary of the ionomer, oxygen, and carbon. Consequently, the utilization of active sites and the performance of catalysts can be further improved when an optimal I/C ratio is employed.²² The utilization of catalysts could not be further improved by using excessive ionomer, which only increases the thickness of the ionomer film, leading to high local transport resistance and flooding. In addition, the extra amount of ionomer could block the pores in the electrode. The effect of the primary catalyst size on MEA performance was also studied (**Figure 6d**). The catalyst with a size of 85 nm demonstrated the best performance due to the uniform distribution of particles (**Figure S25**), improving the ionomer dispersion and catalyst utilization. Both 30 nm and 200 nm catalysts showed poor MEA performance. Large aggregates were observed for the 30 nm catalyst, which prohibited the ionomer from infiltrating into the bulk particles. The majority of the ionomer was usually located around the aggregates, and the interior of the catalyst aggregates lacked ionomer. Even though the 200 nm particles were well distributed, its low ORR activity and low surface area inhibited the MEA performance. Moreover, the ionomer film thickness would be significantly increased if the primary particle size was increased up to 200 nm, which reduced the mass transport dramatically.²² Maximum power density and current density at 0.7 V for all reported iron-free catalysts are summarized in **Figure 6e** and **Table S6**. The new Mn-N-C catalyst shows the most promising performance to replace iron-based catalysts under realistic H₂-air conditions for fuel cell applications.

The MEA durability test of the Mn-N-C-HCl-800/1100 catalyst was also carried out. The cell was tested at a constant voltage of 0.65 V for 160 hours. The performance loss is shown in **Figure S26**, in which 80% activity was retained after the first 16 hours, outperforming most of Fe-free

cathode catalysts (**Table S6**). After 100 hours, more than 50% activity was maintained, demonstrating moderate performance degradation under harsh conditions. The degradation rate was calculated per every 20 hours (**Table S7**). The significant performance loss occurred in the first 20 hours with a decay rate of $1.26 \text{ mA cm}^{-2} \text{ h}^{-1}$. After around 40 hours, the degradation rate became minimal. For comparison, a Fe-N-C catalyst with well-defined FeN_4 sites reported by our group was tested under the same condition (**Figure 6f**).¹¹ The Fe-N-C catalyst exhibited a much faster degradation rate, which is more than twice that of the Mn catalysts. The fast degradation at the initial phase can be mainly attributed to the metal leaching caused by bond breaking between the metal center and adjacent nitrogen atoms. The much faster degradation of the Fe-N-C catalyst was associated with the fragile nature of the Fe-N bond as elucidated by using DFT studies. The new Mn-N-C catalyst could be more durable than Fe-N-C catalysts due to the robust nature of MnN_4 sites as well as enhanced resistance of carbon corrosion. By comparing the carbon structure of those Mn- and Fe-N-C catalysts, a more predominantly graphitic carbon structure was observed for the Mn-N-C catalyst (**Figure S27**).

The durability issue is the grand challenge for M-N-C catalysts compared with PGM catalysts, especially at high voltages ($>0.6 \text{ V}$). The possible causes of M-N-C catalyst degradation were studied in fuel cell cathodes, including the dissolution of MN_4 active sites, carbon oxidation, and the collapse of the three-phase boundary. Based on these mechanisms, the correlated efforts should be focused on the enhancement of the M-N bond by modifying the coordination environment and improvement of carbon materials by increasing the graphitic structure at both atomic and macroscopic levels.⁶³⁻⁶⁴ Moreover, the MEA fabrication techniques can mitigate the performance loss by effectively creating robust three-phase interfaces.

3. Conclusions.

In summary, a new atomically dispersed Mn-N-C ORR catalyst was developed by using an aqueous solution synthesis method via a two-step doping-adsorption approach. Distinguished from prior studies, the effective acid-assisted aqueous solution method combined with a step-pyrolysis (800 °C and 1100 °C) enables curved surface and porous structures of the Mn-N-C catalyst. In addition to low-cost and environmental feasibility, aqueous synthesis leads to an extremely high surface area of the Mn catalysts ($1511 \text{ m}^2 \text{ g}^{-1}$), which is favorable for hosting atomically dispersed single metal sites.

The atomically dispersed nitrogen-coordinated Mn sites were directly visualized and verified by using HAADF-STEM coupled with EELS at the atomic level. XAS results indicated that the Mn ions had a 2+ valence and were coordinated by four N atoms. Remarkable activity and stability of the Mn-N-C catalyst were first confirmed by using RDE in acidic media. The enhanced stability is due to the robust nature of the MnN_4 structure and the high corrosion resistance of its graphitic carbon structure. Additionally, this enhanced stability of MnN_4 was also elucidated by using DFT calculations, in which MnN_4 showed higher resistance to metal leaching than FeN_4 . The Mn-N-C cathode catalysts also demonstrated promising fuel cell performance in MEAs. The maximum power density for this catalyst was 0.39 W cm^{-2} under practical H_2 -air conditions representing the most promising Fe- and PGM-free cathode catalysts. The improved MEA stability of the Mn-N-C catalyst was also observed via a constant voltage test under realistic H_2 -air conditions.

One of the unique features of the Mn-N-C catalyst is the curved surface morphology, which can provide increased external surface and abundant mesopores/macropores. Moreover, the graphitic structure in the catalyst significantly enhances carbon corrosion resistance during the ORR, thus leading to improved stability when compared to other M-N-C catalysts. This work highlights that

the atomic MnN₄ site catalyst can be prepared from the environmentally benign aqueous solution with remarkable activity and stability. The atomically dispersed Mn-N-C catalyst, free of Fe and PGMs, holds great promise for future PEMFCs and other advanced electrocatalysis such as CO₂ reduction⁶⁵ and nitrogen reduction.⁶⁶

ASSOCIATED CONTENT

THE SUPPORTING INFORMATION IS AVAILABLE FREE OF CHARGE ON THE ACS PUBLICATIONS WEBSITE.

Synthetic procedures, material characterization methods, electrochemical measurements, fuel cell tests, computational methods, and additional electrochemical and physical characterization

AUTHOR INFORMATION

Corresponding Authors

Corresponding authors: gangwu@buffalo.edu (G. Wu); guw8@pitt.edu (G.F. Wang); hxu@ginerinc.com (H. Xu).

The authors do not have a conflict of interest

ACKNOWLEDGMENT

We are grateful for the financial support from the U.S. Department of Energy, Fuel Cell Technologies Office (DE-EE0008075) and the ElectroCat Consortium. This research used beamline 7-BM (QAS) of the National Synchrotron Light Source II, a U.S. Department of Energy (DOE) Office of Science User Facility operated for the DOE Office of Science by Brookhaven National Laboratory. The DFT calculations used the computational resources provided by the

University of Pittsburgh Center for Research Computing and the Extreme Science and Engineering Discovery Environment (XSEDE) supported by the National Science Foundation grant number ACI-1053575.

REFERENCES

1. He, Y.; Liu, S.; Priest, C.; Shi, Q.; Wu, G., Atomically dispersed metal–nitrogen–carbon catalysts for fuel cells: advances in catalyst design, electrode performance, and durability improvement. *Chem. Soc. Rev.* **2020**, *49* (11), 3484-3524
2. Wang, X. X.; Swihart, M. T.; Wu, G., Achievements, challenges and perspectives on cathode catalysts in proton exchange membrane fuel cells for transportation. *Nat. Catal.* **2019**, *2* (7), 578-589.
3. Hou, J.; Yang, M.; Ke, C.; Wei, G.; Priest, C.; Qiao, Z.; Wu, G.; Zhang, J., Platinum-group-metal catalysts for proton exchange membrane fuel cells: From catalyst design to electrode structure optimization. *EnergyChem* **2020**, *2* (1), 100023.
4. Li, Y.; Wang, H.; Priest, C.; Li, S.; Xu, P.; Wu, G., Advanced Electrocatalysis for Energy and Environmental Sustainability via Water and Nitrogen Reactions. *Adv. Mater.* **2020**, *n/a* (10.1002/adma.202000381), 2000381.
5. Lefèvre, M.; Proietti, E.; Jaouen, F.; Dodelet, J.-P., Iron-based catalysts with improved oxygen reduction activity in polymer electrolyte fuel cells. *Science* **2009**, *324* (5923), 71-74.
6. Wu, G.; More, K. L.; Johnston, C. M.; Zelenay, P., High-Performance Electrocatalysts for Oxygen Reduction Derived from Polyaniline, Iron, and Cobalt. *Science* **2011**, *332* (6028), 443-447.
7. Chen, M.; He, Y.; Spendelow, J. S.; Wu, G., Atomically Dispersed Metal Catalysts for Oxygen Reduction. *ACS Energy Lett.* **2019**, *4* (7), 1619-1633.
8. He, Y.; Tan, Q.; Lu, L.; Sokolowski, J.; Wu, G., Metal-Nitrogen-Carbon Catalysts for Oxygen Reduction in PEM Fuel Cells: Self-Template Synthesis Approach to Enhancing Catalytic Activity and Stability. *Electrochem. Energy Rev.* **2019**, *2* (2), 231-251.
9. Wan, X.; Liu, X.; Li, Y.; Yu, R.; Zheng, L.; Yan, W.; Wang, H.; Xu, M.; Shui, J., Fe–N–C electrocatalyst with dense active sites and efficient mass transport for high-performance proton exchange membrane fuel cells. *Nat. Catal.* **2019**, *2* (3), 259.
10. Zhang, H.; Chung, H. T.; Cullen, D. A.; Wagner, S.; Kramm, U. I.; More, K. L.; Zelenay, P.; Wu, G., High-performance fuel cell cathodes exclusively containing atomically dispersed iron active sites. *Energy Environ. Sci.* **2019**, *12* (8), 2548-2558.
11. Zhang, H.; Hwang, S.; Wang, M.; Feng, Z.; Karakalos, S.; Luo, L.; Qiao, Z.; Xie, X.; Wang, C.; Su, D.; Shao, Y.; Wu, G., Single Atomic Iron Catalysts for Oxygen Reduction in Acidic Media: Particle Size Control and Thermal Activation. *J. Am. Chem. Soc.* **2017**, *139* (40), 14143-14149.

12. Martinez, U.; Komini Babu, S.; Holby, E. F.; Chung, H. T.; Yin, X.; Zelenay, P., Progress in the Development of Fe-Based PGM-Free Electrocatalysts for the Oxygen Reduction Reaction. *Adv. Mater.* **2019**, *31* (31), 1806545.
13. Asset, T.; Atanassov, P., Iron-Nitrogen-Carbon Catalysts for Proton Exchange Membrane Fuel Cells. *Joule* **2020**, *4* (1), 33-44.
14. Wang, X. X.; Prabhakaran, V.; He, Y.; Shao, Y.; Wu, G., Iron - Free Cathode Catalysts for Proton - Exchange - Membrane Fuel Cells: Cobalt Catalysts and the Peroxide Mitigation Approach. *Adv. Mater.* **2019**, 1805126.
15. Wang, X. X.; Cullen, D. A.; Pan, Y. T.; Hwang, S.; Wang, M.; Feng, Z.; Wang, J.; Engelhard, M. H.; Zhang, H.; He, Y., Nitrogen - Coordinated Single Cobalt Atom Catalysts for Oxygen Reduction in Proton Exchange Membrane Fuel Cells. *Adv. Mater.* **2018**, *30* (11), 1706758.
16. He, Y.; Hwang, S.; Cullen, D. A.; Uddin, M. A.; Langhorst, L.; Li, B.; Karakalos, S.; Kropf, A. J.; Wegener, E. C.; Sokolowski, J.; Chen, M.; Myers, D.; Su, D.; More, K. L.; Wang, G.; Litster, S.; Wu, G., Highly active atomically dispersed CoN₄ fuel cell cathode catalysts derived from surfactant-assisted MOFs: carbon-shell confinement strategy. *Energy Environ. Sci.* **2019**, *12* (1), 250-260.
17. Gubler, L.; Dockheer, S. M.; Koppenol, W. H., Radical (HO•, H• and HOO•) formation and ionomer degradation in polymer electrolyte fuel cells. *J. Electrochem. Soc.* **2011**, *158* (7), B755-B769.
18. Borup, R.; Meyers, J.; Pivovar, B.; Kim, Y. S.; Mukundan, R.; Garland, N.; Myers, D.; Wilson, M.; Garzon, F.; Wood, D.; Zelenay, P.; More, K.; Stroh, K.; Zawodzinski, T.; Boncella, J.; McGrath, J. E.; Inaba, M.; Miyatake, K.; Hori, M.; Ota, K.; Ogumi, Z.; Miyata, S.; Nishikata, A.; Siroma, Z.; Uchimoto, Y.; Yasuda, K.; Kimijima, K.-i.; Iwashita, N., Scientific Aspects of Polymer Electrolyte Fuel Cell Durability and Degradation. *Chem. Rev.* **2007**, *107* (10), 3904-3951.
19. Thompson, S. T.; Wilson, A. R.; Zelenay, P.; Myers, D. J.; More, K. L.; Neyerlin, K.; Papageorgopoulos, D., ElectroCat: DOE's approach to PGM-free catalyst and electrode R&D. *Solid State Ionics* **2018**, *319*, 68-76.
20. Li, J.; Chen, M.; Cullen, D. A.; Hwang, S.; Wang, M.; Li, B.; Liu, K.; Karakalos, S.; Lucero, M.; Zhang, H.; Lei, C.; Xu, H.; Sterbinsky, G. E.; Feng, Z.; Su, D.; More, K. L.; Wang, G.; Wang, Z.; Wu, G., Atomically dispersed manganese catalysts for oxygen reduction in proton-exchange membrane fuel cells. *Nat. Catal.* **2018**, *1* (12), 935-945.
21. Liu, K.; Qiao, Z.; Hwang, S.; Liu, Z.; Zhang, H.; Su, D.; Xu, H.; Wu, G.; Wang, G., Mn-and N-doped carbon as promising catalysts for oxygen reduction reaction: Theoretical prediction and experimental validation. *Appl. Catal. B Environ.* **2019**, *243*, 195-203.
22. Uddin, A.; Dunsmore, L.; Zhang, H.; Hu, L.; Wu, G.; Litster, S., High Power Density Platinum Group Metal-free Cathodes for Polymer Electrolyte Fuel Cells. *ACS Appl. Mater. Interfaces* **2019**, *12* (2), 2216-2224.
23. Zhao, X.; Yang, X.; Wang, M.; Hwang, S.; Karakalos, S.; Chen, M.; Qiao, Z.; Wang, L.; Liu, B.; Ma, Q.; Cullen, D. A.; Su, D.; Yang, H.; Zang, H.-Y.; Feng, Z.; Wu, G., Single-Iron

Site Catalysts with Self-Assembled Dual-size Architecture and Hierarchical Porosity for Proton-Exchange Membrane Fuel Cells. *Appl. Catal. B Environ.* **2020**, 119400.

24. Li, J.; Zhang, H.; Samarakoon, W.; Shan, W.; Cullen, D. A.; Karakalos, S.; Chen, M.; Gu, D.; More, K. L.; Wang, G.; Feng, Z.; Wang, Z.; Wu, G., Thermally Driven Structure and Performance Evolution of Atomically Dispersed FeN₄ Sites for Oxygen Reduction. *Angew. Chem. Int. Ed.* **2019**, *58* (52), 18971-18980.
25. Chung, H. T.; Cullen, D. A.; Higgins, D.; Sneed, B. T.; Holby, E. F.; More, K. L.; Zelenay, P., Direct atomic-level insight into the active sites of a high-performance PGM-free ORR catalyst. *Science* **2017**, *357* (6350), 479-484.
26. Zitolo, A.; Goellner, V.; Armel, V.; Sougrati, M.-T.; Mineva, T.; Stievano, L.; Fonda, E.; Jaouen, F., Identification of catalytic sites for oxygen reduction in iron-and nitrogen-doped graphene materials. *Nat. Mater.* **2015**, *14* (9), 937-945.
27. Zhang, H.; Osgood, H.; Xie, X.; Shao, Y.; Wu, G., Engineering nanostructures of PGM-free oxygen-reduction catalysts using metal-organic frameworks. *Nano Energy* **2017**, *31*, 331-350.
28. Wang, X. X.; Hwang, S.; Pan, Y.-T.; Chen, K.; He, Y.; Karakalos, S.; Zhang, H.; Spendelow, J. S.; Su, D.; Wu, G., Ordered Pt₃Co Intermetallic Nanoparticles Derived from Metal–Organic Frameworks for Oxygen Reduction. *Nano Letters* **2018**, *18* (7), 4163-4171.
29. Mukherjee, S.; Cullen, D. A.; Karakalos, S.; Liu, K.; Zhang, H.; Zhao, S.; Xu, H.; More, K. L.; Wang, G.; Wu, G., Metal-organic framework-derived nitrogen-doped highly disordered carbon for electrochemical ammonia synthesis using N₂ and H₂O in alkaline electrolytes. *Nano Energy* **2018**, *48*, 217-226.
30. Cravillon, J.; Münzer, S.; Lohmeier, S.-J.; Feldhoff, A.; Huber, K.; Wiebcke, M., Rapid room-temperature synthesis and characterization of nanocrystals of a prototypical zeolitic imidazolate framework. *Chem. Mater.* **2009**, *21* (8), 1410-1412.
31. Zhang, H.; Li, J.; Tan, Q.; Lu, L.; Wang, Z.; Wu, G., Metal–Organic Frameworks and Their Derived Materials as Electrocatalysts and Photocatalysts for CO₂ Reduction: Progress, Challenges, and Perspectives. *Chem. Eur. J.* **2018**, *24* (69), 18137-18157.
32. Crawford, D.; Casaban, J.; Haydon, R.; Giri, N.; McNally, T.; James, S. L., Synthesis by extrusion: continuous, large-scale preparation of MOFs using little or no solvent. *Chem. Sci.* **2015**, *6* (3), 1645-1649.
33. Pan, Y.; Liu, Y.; Zeng, G.; Zhao, L.; Lai, Z., Rapid synthesis of zeolitic imidazolate framework-8 (ZIF-8) nanocrystals in an aqueous system. *Chem. Comm.* **2011**, *47* (7), 2071-2073.
34. Zhao, X.; Chen, M.; Zuo, J.; Wang, J.; Liu, Z.; Wang, L.; Liu, B.; Wu, G.; Zhang, H.; Yang, H., Fe-Doped Metal-Organic Frameworks-Derived Electrocatalysts for Oxygen Reduction Reaction in Alkaline Media. *J. Electrochem. Soc.* **2018**, *165* (16), F1278-F1285.
35. Salunkhe, R. R.; Young, C.; Tang, J.; Takei, T.; Ide, Y.; Kobayashi, N.; Yamauchi, Y., A high-performance supercapacitor cell based on ZIF-8-derived nanoporous carbon using an organic electrolyte. *Chem. Comm.* **2016**, *52* (26), 4764-4767.

36. Dissegna, S.; Epp, K.; Heinz, W. R.; Kieslich, G.; Fischer, R. A., Defective Metal - Organic Frameworks. *Adv. Mater.* **2018**, *30* (37), 1704501.
37. Vinu, M.; Raja, D. S.; Jiang, Y.-C.; Liu, T.-Y.; Xie, Y.-Y.; Lin, Y.-F.; Yang, C.-C.; Lin, C.-H.; Alshehri, S. M.; Ahamad, T., Effects of structural crystallinity and defects in microporous Al-MOF filled chitosan mixed matrix membranes for pervaporation of water/ethanol mixtures. *J. Taiwan Inst. Chem. E* **2018**, *83*, 143-151.
38. Wang, H.; Kong, D.; Johanes, P.; Cha, J. J.; Zheng, G.; Yan, K.; Liu, N.; Cui, Y., MoSe₂ and WSe₂ nanofilms with vertically aligned molecular layers on curved and rough surfaces. *Nano Lett.* **2013**, *13* (7), 3426-3433.
39. Kibsgaard, J.; Chen, Z.; Reinecke, B. N.; Jaramillo, T. F., Engineering the surface structure of MoS₂ to preferentially expose active edge sites for electrocatalysis. *Nat. Mater.* **2012**, *11* (11), 963.
40. Cheng, P.; Hu, Y. H., H₂O-functionalized zeolitic Zn (2-methylimidazole)₂ framework (ZIF-8) for H₂ storage. *J. Phys. Chem. C* **2014**, *118* (38), 21866-21872.
41. Jaouen, F.; Herranz, J.; Lefevre, M.; Dodelet, J.-P.; Kramm, U. I.; Herrmann, I.; Bogdanoff, P.; Maruyama, J.; Nagaoka, T.; Garsuch, A., Cross-laboratory experimental study of non-noble-metal electrocatalysts for the oxygen reduction reaction. *ACS Appl. Mater. Interfaces* **2009**, *1* (8), 1623-1639.
42. Proietti, E.; Jaouen, F.; Lefèvre, M.; Larouche, N.; Tian, J.; Herranz, J.; Dodelet, J.-P., Iron-based cathode catalyst with enhanced power density in polymer electrolyte membrane fuel cells. *Nat. Comm.* **2011**, *2*, 416.
43. Jaouen, F.; Lefèvre, M.; Dodelet, J.-P.; Cai, M., Heat-treated Fe/N/C catalysts for O₂ electroreduction: are active sites hosted in micropores? *J. Phys. Chem. B* **2006**, *110* (11), 5553-5558.
44. Chlistunoff, J., RRDE and voltammetric study of ORR on pyrolyzed Fe/polyaniline catalyst. On the origins of variable Tafel slopes. *J. Phys. Chem. C* **2011**, *115* (14), 6496-6507.
45. Li, Y.; Zhou, W.; Wang, H.; Xie, L.; Liang, Y.; Wei, F.; Idrobo, J.-C.; Pennycook, S. J.; Dai, H., An oxygen reduction electrocatalyst based on carbon nanotube-graphene complexes. *Nat. Nanotech.* **2012**, *7* (6), 394.
46. Holewinski, A.; Linic, S., Elementary mechanisms in electrocatalysis: revisiting the ORR Tafel slope. *J. Electrochem. Soc.* **2012**, *159* (11), H864-H870.
47. Qiao, Z.; Hwang, S.; Li, X.; Wang, C.; Samarakoon, W.; Karakalos, S.; Li, D.; Chen, M.; He, Y.; Wang, M.; Liu, Z.; Wang, G.; Zhou, H.; Feng, Z.; Su, D.; Spendelow, J. S.; Wu, G., 3D porous graphitic nanocarbon for enhancing the performance and durability of Pt catalysts: a balance between graphitization and hierarchical porosity. *Energy Environ. Sci.* **2019**, *12* (9), 2830-2841.
48. Gupta, S.; Zhao, S.; Wang, X. X.; Hwang, S.; Karakalos, S.; Devaguptapu, S. V.; Mukherjee, S.; Su, D.; Xu, H.; Wu, G., Quaternary FeCoNiMn-Based Nanocarbon Electrocatalysts for Bifunctional Oxygen Reduction and Evolution: Promotional Role of Mn Doping in Stabilizing Carbon. *ACS Catal.* **2017**, *7* (12), 8386-8393.

49. Nuithitikul, K.; Srikhun, S.; Hirunpraditkoon, S., Influences of pyrolysis condition and acid treatment on properties of durian peel-based activated carbon. *Bioresour. Technol.* **2010**, *101* (1), 426-429.
50. Park, S.-J.; Kim, K.-D., Adsorption Behaviors of CO₂ and NH₃ on Chemically Surface-Treated Activated Carbons. *J. Colloid Interface Sci.* **1999**, *212* (1), 186-189.
51. Xiao, W.; Miao, C.; Yin, X.; Zheng, Y.; Tian, M.; Li, H.; Mei, P., Effect of urea as pore-forming agent on properties of poly (vinylidene fluoride-co-hexafluoropropylene)-based gel polymer electrolyte. *J. Power Sources* **2014**, *252*, 14-20.
52. Jurkiewicz, K.; Pawlyta, M.; Zygadło, D.; Chrobak, D.; Duber, S.; Wrzalik, R.; Ratuszna, A.; Burian, A., Evolution of glassy carbon under heat treatment: correlation structure–mechanical properties. *J. Mater. Sci.* **2018**, *53* (5), 3509-3523.
53. Wen, J.; Zeng, Z.; Yang, L.; Zeng, Q.; Lou, H.; Sheng, H.; Miller, D. J.; Yang, W.; Mao, H.-k., TEM Study of Amorphous Carbon with Fully sp³-Bonded Structure. *Microsc. Microanal.* **2017**, *23* (S1), 2268-2269.
54. Sharma, S.; Kumar, C. S.; Korvink, J. G.; Kübel, C., Evolution of glassy carbon microstructure: in situ transmission electron microscopy of the pyrolysis process. *Sci. Rep.* **2018**, *8* (1), 16282.
55. Chen, Y.; Ji, S.; Chen, C.; Peng, Q.; Wang, D.; Li, Y., Single-atom catalysts: Synthetic strategies and electrochemical applications. *Joule* **2018**, *2* (7), 1242-1264.
56. Xia, D.; Yang, X.; Xie, L.; Wei, Y.; Jiang, W.; Dou, M.; Li, X.; Li, J.; Gan, L.; Kang, F., Direct Growth of Carbon Nanotubes Doped with Single Atomic Fe–N₄ Active Sites and Neighboring Graphitic Nitrogen for Efficient and Stable Oxygen Reduction Electrocatalysis. *Adv. Func. Mater.* **2019**, *29* (49), 1906174.
57. Guan, J.; Duan, Z.; Zhang, F.; Kelly, S. D.; Si, R.; Dupuis, M.; Huang, Q.; Chen, J. Q.; Tang, C.; Li, C., Water oxidation on a mononuclear manganese heterogeneous catalyst. *Nat. Catal.* **2018**, *1* (11), 870-877.
58. Rana, J.; Kloepsch, R.; Li, J.; Scherb, T.; Schumacher, G.; Winter, M.; Banhart, J., On the structural integrity and electrochemical activity of a 0.5 Li₂MnO₃·0.5 LiCoO₂ cathode material for lithium-ion batteries. *J. Mater. Chem. A* **2014**, *2* (24), 9099-9110.
59. Luo, J.-H.; Hong, Z.-S.; Chao, T.-H.; Cheng, M.-J., Quantum Mechanical Screening of Metal-N₄-Functionalized Graphenes for Electrochemical Anodic Oxidation of Light Alkanes to Oxygenates. *J. Phys. Chem. C* **2019**, *123* (31), 19033-19044.
60. Komini Babu, S.; Chung, H. T.; Zelenay, P.; Litster, S., Resolving electrode morphology's impact on platinum group metal-free cathode performance using nano-CT of 3D hierarchical pore and ionomer distribution. *ACS Appl. Mater. Interfaces* **2016**, *8* (48), 32764-32777.
61. Shinozaki, K.; Yamada, H.; Morimoto, Y., Relative humidity dependence of Pt utilization in polymer electrolyte fuel cell electrodes: effects of electrode thickness, ionomer-to-carbon ratio, ionomer equivalent weight, and carbon support. *J. Electrochem. Soc.* **2011**, *158* (5), B467-B475.
62. Padgett, E.; Andrejevic, N.; Liu, Z.; Kongkanand, A.; Gu, W.; Moriyama, K.; Jiang, Y.; Kumaraguru, S.; Moylan, T. E.; Kukreja, R., Connecting Fuel Cell Catalyst Nanostructure

and Accessibility Using Quantitative Cryo-STEM Tomography. *J. Electrochem. Soc.* **2018**, *165* (3), F173-F180.

63. Zhu, Y.; Sokolowski, J.; Song, X.; He, Y.; Mei, Y.; Wu, G., Engineering Local Coordination Environments of Atomically Dispersed and Heteroatom-Coordinated Single Metal Site Electrocatalysts for Clean Energy-Conversion. *Adv. Energy Mater.* **2020**, *10* (11), 1902844.
64. Shi, Q.; Hwang, S.; Yang, H.; Ismail, F.; Su, D.; Higgins, D.; Wu, G., Supported and coordinated single metal site electrocatalysts. *Mater. Today* **2020**, 10.1016/j.mattod.2020.02.019.
65. Pan, F.; Zhang, H.; Liu, K.; Cullen, D.; More, K.; Wang, M.; Feng, Z.; Wang, G.; Wu, G.; Li, Y., Unveiling Active Sites of CO₂ Reduction on Nitrogen-Coordinated and Atomically Dispersed Iron and Cobalt Catalysts. *ACS Catalysis* **2018**, *8* (4), 3116-3122.
66. Mukherjee, S.; Yang, X.; Shan, W.; Samarakoon, W.; Karakalos, S.; Cullen, D. A.; More, K.; Wang, M.; Feng, Z.; Wang, G.; Wu, G., Atomically Dispersed Single Ni Site Catalysts for Nitrogen Reduction toward Electrochemical Ammonia Synthesis Using N₂ and H₂O. *Small Methods* **2020**, *4* (6), 1900821.